water

MDPI

Article

Visible Light Photocatalyst and Antibacterial Activity of BFO (Bismuth Ferrite) Nanoparticles from Honey

M. Sharmila [1,*], R. Jothi Mani [2], C. Parvathiraja [3], S. M. Abdul Kader [4], Masoom Raza Siddiqui [5], Saikh Mohammad Wabaidur [5], Md Ataul Islam [6] and Wen-Cheng Lai [7,8,*]

1 Research Scholar (18211192132009), Department of Physics, Sadakathullah Appa College, Affiliated to Manonmaniam Sundarnar University, Tirunelveli 627012, Tamilnadu, India
2 Assistant Professor, Department of Physics, Fatima College, Madurai 625018, Tamilnadu, India; drjothifatima@gmail.com
3 Department of Physics, Manonmaniam Sundaranar University, Tirunelveli 627012, Tamilnadu, India; cpraja1206@gmail.com
4 Department of Physics, Sadakathullah Appa College, Tirunelveli 627011, Tamilnadu, India; smabdulkader@sadakath.ac.in
5 Chemistry Department, College of Science, King Saud University, Riyadh 11451, Saudi Arabia; siddiqui124@gmail.com (M.R.S.); swabaidur@ksu.edu.sa (S.M.W.)
6 Division of Pharmacy and Optometry, School of Health Sciences, Faculty of Biology, Medicine and Health, University of Manchester, Manchester M13 9PL, UK; ataul.islam80@gmail.com
7 Bachelor Program in Industrial Projects, National Yunlin University of Science and Technology, Douliu 640301, Taiwan
8 Department of Electronic Engineering, National Yunlin University of Science and Technology, Douliu 640301, Taiwan
* Correspondence: msharmilaphysics@sadakath.ac.in (M.S.); wenlai@yuntech.edu.tw or wenlai@mail.ntust.edu.tw (W.-C.L.)

check for updates

Citation: Sharmila, M.; Mani, R.J.; Parvathiraja, C.; Kader, S.M.A.; Siddiqui, M.R.; Wabaidur, S.M.; Islam, M.A.; Lai, W.-C. Visible Light Photocatalyst and Antibacterial Activity of BFO (Bismuth Ferrite) Nanoparticles from Honey. *Water* **2022**, *14*, 1545. https://doi.org/10.3390/w14101545

Academic Editors: Mika Sillanpää and Peyman Gholami

Received: 12 April 2022
Accepted: 10 May 2022
Published: 11 May 2022

Publisher's Note: MDPI stays neutral with regard to jurisdictional claims in published maps and institutional affiliations.

Abstract: Visible light-driven photocatalyst $BiFeO_3$ (BFO) nanoparticles were synthesised by the auto-combustion method. The honey was used to fuel the auto combustion method to synthesise the BFO nanoparticles. The structural, optical and morphological activities of the bismuth loaded BFO nanoparticles were characterised by X-ray diffraction (XRD), FTIR, UV, photoluminescence (PL) and SEM analysis, respectively. The bismuth content modifies the lattice parameters of XRD and reduces the bandgap energy. The observed crystallite size varies from 19 to 27 nm and the bandgap region is 2.07 to 2.21 eV. The photo-charge carriers increased upon the BFO nanoparticles and their emission at 587 nm in the visible region of the PL spectrum. The 2% bismuth loaded BFO nanoparticles showed better morphology than 0% and 5% bismuth loaded BFO nanoparticles. The oxidation state of BFO nanoparticles and their binding energies were characterised by X-ray Photoelectron Spectroscopy (XPS) analysis. The methylene blue dye (MB) degradation against 2% BFO nanoparticles showed enhanced catalytic activity (81%) than the remaining samples of BFO nanoparticles. The bacterial activity of BFO nanoparticles was assessed against Gram-positive and Gram-negative bacteria, including *S. aureus* and *E. coli*. 2% Excess bismuth BFO nanoparticles exhibit better antibacterial activity. Comparatively, 2% Excess bismuth BFO nanoparticles derived an outstanding crystallinity, charge separation, and reduced bandgap activities. Based on these findings, BFO nanoparticles may be applicable in drug delivery and water remediation applications.

Keywords: BFO; visible light; honey; green synthesis and photocatalysis

1. Introduction

Magnetic nanoparticles possess multiple applications due to their large number of oxides with reasonable magnetic properties. Their applications are sensors, solar energy devices and data storage. These applications are very basic applications of ferrites [1]. Various numbers of metal ferrite oxides are available; they are NFO (Nickel Ferrite), ZFO

(Zinc Ferrite) and BFO (Bismuth Ferrite). Among these metal ferrite oxides, BFO possesses unique electrical and magnetic properties, reasonable visible-light responsive photo-catalyst properties, and also having good binding energy, lithium-ion batteries, enriched chemical stability and field emission properties [2]. Bismuth ferrite has an orthorhombic structure and also it is essential among the other type of iron oxides. Bismuth ferrite possess a high curie temperature (T_c = 1103 K) and Neel temperature (T_N = 643 K) [3]. Various type of synthesis methods of BFO are available including solution combustion [4], combustion reaction [5], co-precipitation [6], molten salt [7], sol-gel [8], microwave synthesis [9], electrospinning [10], solvothermal [11], pechini [12], hydrothermal [13], sonochemical [14] and solution evaporation [15]. Among all these types of syntheses, green synthesis gives the best result. The perovskite Bismuth Ferrite, $BiFeO_3$, is one of the most promising materials in the field of multiferroics. The contribution of both ferroelectric and ferromagnetic properties in its switchable domain tends to bring out a revolution in memory storage applications. Many more potential applications, such as in solar cells as an effect of the smaller bandgap, photocatalytic activity due to its absorption in the visible region, gas sensors, water splitting, etc., make the researchers show a lot of interest in this $BiFeO_3$ material. However, it suffers from the following problems: (i) presence of impurity phases, (ii) low remnant polarisation and remnant magnetisation, (iii) high leakage current, (iv) wide gap between the transition temperatures and (v) weak magnetoelectric coupling. All these problems are related to the challenge of forming phase pure $BiFeO_3$. Even after using various techniques to overcome this issue in the last decade, it is still a challenging one. From the literature survey, we have found that the Phase fuel plays a vital role in forming up $BiFeO_3$ in its pure form. One of the common problems all over the world is water contamination. These water contaminations have four types: radiological contaminants, organic contaminants, inorganic contaminants, and biological contaminants. Now we focus on the organic contaminants; the major sources of organic contamination are industrial waste, pesticides and domestic waste [16]. Many industries use organic dyes, but they are heavy pollutants to our environment and they cause more health issues to human beings [17–21]. Nowadays, many researchers provide more importance to producing nanoparticles from the green synthesis method. The green synthesised nanoparticles effectively eliminate the organic dyes from wastewater [22]. Honey has many practical applications in the medical field due to its derivatives of carbohydrates, vitamins and amino acids. Their derivatives cure many diseases directly and indirectly and their products can control nanoparticle growth and sizes. BFO have a narrow band gap energy, multiferroic behaviour and their photocatalytic activity successfully degrade the toxic and biological pollutants [23]. Therefore, in our present work, we have synthesised $BiFeO_3$ using a novel combustion technique without using any acid or harmful products. The green way nano-production is a non-toxic synthesis protocol and their existing bio-compounds induce the antimicrobial activity in the biological system. The results were analysed using XRD, UV-vis spectra, FTIR, and PL. Bandgap values derived from the UV-Vis spectral data fall in the visible region and it demonstrates the possibility of practical applications. The synthesised BFO nanoparticles were examined in MB dye solution and bacterial activity studies.

2. Materials and Methods

2.1. Materials

The synthesising materials purchased from Himedia AR grade and used to prepare $BiFeO_3$ were bismuth nitrate Bi $(NO3)_3$ $5H_2O$, iron nitrate Fe $(NO3)_3$ $9H_2O$ and honey solution were procured from siddha medical store, Tirunelvei, Tamilnadu, India.

2.2. Experimental Section

Bi $(NO_3)_3$ $5H_2O$, Fe $(NO_3)_3$ $9H_2O$ were used as precursors. Bismuth nitrate (0.2 M) and Iron nitrate (0.2 M) were taken in stoichiometric ratio and dissolved in water containing 3 mL of Honey. To this homogenous mixture, an excess amount of bismuth was added in the following percentage 0%, 2% and 5%. Then the solution was stirred for about 2-h

at room temperature. After 2-h of stirring, the solution was dried at 180 °C in the oven overnight. Finally, the dried powder was preheated at 450 °C for 10 min and annealed at 600 °C for 2-h to obtain the required $BiFeO_3$ nanoparticles. The detailed synthesis protocol of BFO nanoparticles is displayed in Scheme 1.

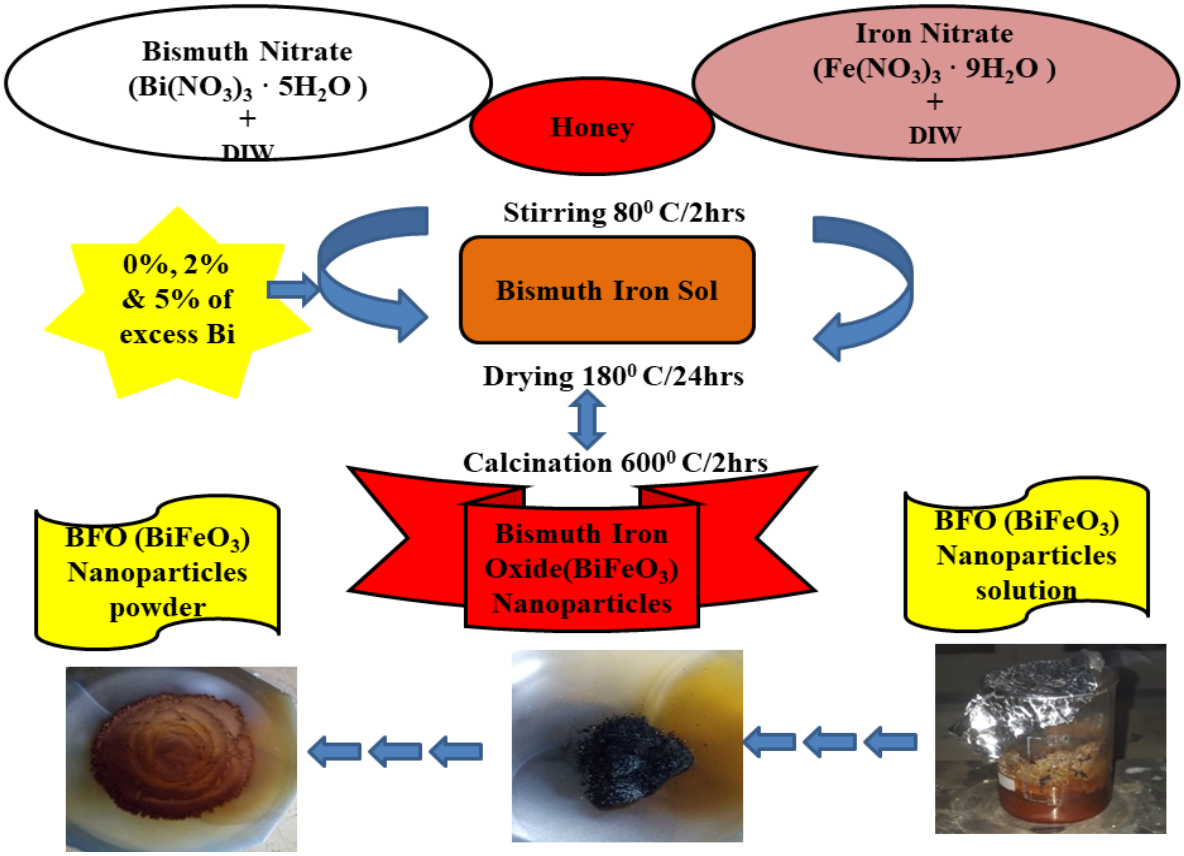

Scheme 1. Synthesis protocol of BFO (0%, 2% and 5% Excess Bi) nanoparticles.

2.3. Characterisation

The crystalline nature of the synthesised nanoparticles was evaluated from XPERT PRO PANalytical X-ray diffractometer functioning at 40 KV, 30 mA with Cu Kα radiation. The functional group were observed from the FTIR Spectrometer (Perkin-Elmer 1725X) (Waltham, MA, USA). The optical and electronic details were attained from the UV-DRS spectrum (UV/Vis DRS Spectrometer Shimadzu-2700) (Kyoto, Japan) and photoluminescence spectra (spectrofluorometer PC1 (ISS, Austin, TX, USA)). The surface morphology of the nanoparticles was carried out by (FESEM) ZEISS, SIGMA. The chemical compositions and their binding between the energised particles were observed from XPS (XPS-PHI 5000, Austin, TX, USA)

2.4. Antibacterial Activity

The bacterial strain *Staphylococcus aureus* and *Escherichia coli* were used to evaluate the antibacterial activity of the title compound by using the disc diffusion method. The Muller-Hinton broth was used for bacteria cultured overnight. Then the growing bacteria was spread to the sterilised Petri plates (100 µL × 10^{-7} cm CFU). The 6 mm diameter disc was filled with BFO nanoparticles (50 µg). Finally, the loaded Petri plates were incubated at 37 °C (overnight). The zone of inhibitions gives the bacterial susceptibility of the BFO nanoparticles and their zone was calculated on an mm scale. The obtained inhibitions were compared with amoxicillin (US Antibiotics) and honey solution.

2.5. Photocatalytic Activity

The MB dye is used as a model effluent to degrade the organic compounds. The 100 mL organic compound (MB = 30 mg/L) and BFO nanomaterials (10 mg) were placed in a dark condition with continuous stirring. The dark condition induces the adsorption-desorption equilibrium position of the combined solution. The visible light (above 400 nm) irradiated photocatalyst samples were withdrawn at regular time intervals of 30 min. The taken samples were then centrifuged for 10,000 rpm (3 times) to remove the catalyst and filtered in Whatman No.1 filter paper. The supernatant solution emanates dye degradation activity of BFO nanoparticles. The dissociation percentage of the dye molecules was calculated by the following equations.

$$\text{Dye degradation } (\%) = \frac{C_0 - C_t}{C_0} \times 100$$

where C_0 is the initial dye concentration and C_t is the light irradiated dye concentration.

3. Results and Discussions

3.1. XRD Analysis

The X-ray diffraction pattern of BFO nanoparticles is shown in Figure 1. The figure denotes the various amount of bismuth content in the BFO nanoparticles. Figure 1 also shows the XRD results of 0%, 2% and 5% of excess bismuth added for the compound formation and compared with the standard JCPDS No: 71-2494. The excessive addition of 2% tends to have an impurity lower than the 5%. All the (h k l) planes (012), (104), (110), (202), (024), (116), (122), (018), (214), (300), (125), (208), (220) were indexed and have a good agreement with the JCPDS: 71-2494 [24]. The 0% of excess bismuth in the BFO nanoparticles showed many unwanted peaks and their phase instability had been modified by the addition of 2% and 5% of excess bismuth into the BFO nanoparticles. The 0% excess of Bi content demonstrates the Fe-rich peaks, which does not match with standard BFO pattern and it is not BFO nanoparticles. 5% excess of Bi content provokes the Bi content in BFO nanoparticles. Fe and Bi-enriched BFO nanoparticles are not convinced of the std JCPDS peaks. So, 0% and 5% excess of Bi content BFO nanoparticles presented many unwanted peaks. The excessive amount of bismuth can regulate the phase changes and lattice orientations. Their lattice parameters were found using unit cell software and tabulated in Table 1.

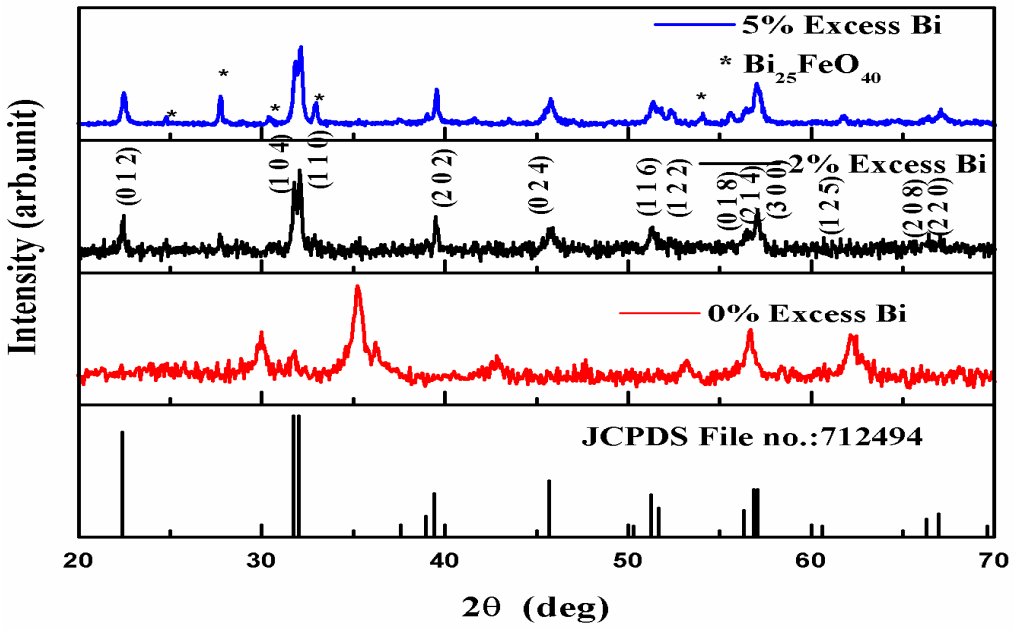

Figure 1. X-ray diffraction pattern of BFO (0%, 2% and 5% Excess Bi) nanoparticles.

Table 1. Cell parameters of $BiFeO_3$ Nanoparticles.

Parameters	Different Precursors of $BiFeO_3$ Nanoparticles Samples		Standard JCPDS File No.: 71-2494
	2%Excess	5%Excess	
a = b (Å)	5.5651	5.5696	5.587
c (Å)	13.8760	13.8714	13.867
V $(Å)^3$	372.1664	372.6507	374.94

The crystalline size, microstrain and dislocation density of the BFO nanoparticles were calculated and their values are listed in Table 2.

Table 2. XRD parameters of $BiFeO_3$ nanoparticles.

Sample Name	Crystallite Size (nm)	Microstrain (m^{-4})	Dislocation Density (m^{-2})
0% Excess	19.2	7.04×10^{-5}	2.71×10^{17}
2% Excess	10.51	1.66×10^{-3}	9.05×10^{17}
5% Excess	26.84	7.04×10^{-4}	1.39×10^{17}

The obtained values of the BFO nanoparticles unveiled the BFO on nanoscale and their values revealed the increase in bismuth content decreased the crystallite size values up to 2% bismuth content. After that, the bismuth content increases the crystallite size. The decreased crystallite size samples initiate the electron mobility and inhibit the e-h pair, which produce the enhanced catalytic reaction [25].

3.2. FTIR Analysis

Figure 2 shows the FTIR spectra of BFO nanoparticles with 0%, 2% and 5% of excess bismuth. The spectrum revealed a noticeable change in their bond vibration and bond stretching. The addition of 2% bismuth gives a better result than 5% or 0% of excessive bismuth. Their transmittance is high and their strong vibration band at 520 cm^{-1} contributes to the stretching and bending of the Fe-O-Fe octahedra structure of BFO [26,27]. The remaining peaks of the 2% bismuth spectrum came from the honey solution. The honey attributes the reduction/capping of BFO nanoparticles. Moreover, 2% excess of bismuth derived an enhanced activity and their surface was encapsulated from honey molecules (insert figure). The prominent peaks at 1117 cm^{-1} are attributed to the vibration of C-N and C-O, which are responsible for the capping of nanoparticles [28–30]. The dotted round-shaped peaks at 855 cm^{-1} and 813 cm^{-1} indicate the existence of bismuth presence in BFO nanoparticles, which increased with respect to Bi [26,27]. The remaining peaks are responsible for the compounds of vitamins, glucose, proteins, fructose, sucrose and minerals. These biomolecules serve multiple actions during the nano production of BFO nanoparticles. The honey molecules encouraged BFO nanoparticle formations and their honey compounds interface with the metal sourced to provide the better catalytic and bacterial activity.

3.3. UV-DRS Analysis

The absorbance spectrum of synthesised BFO nanoparticles is shown in Figure 3a. The raw BFO nanoparticles exhibited the visible region absorption and their value was matched with previous work [31,32]. The visible light absorbance approves the visible light photocatalytic activity and their absorption responds to visible light activity. The excess bismuth BFO nanoparticles' absorbance edge values are enhanced than raw BFO nanoparticles. During the addition of bismuth into the BFO nanoparticles, the absorbance peaks are shifted towards the higher visible region, increasing the intensity with bismuth

content. The spectra are exhibited the strongest absorption peaks in the visible light region, which could be responsible for the enhanced activity of e-h pair recombination [33]. The bandgap calculations were carried out by Kubelka–Munk function whereas, $(\alpha h\nu)^2$ vs. hν (photon energy) for direct bandgap semiconductor as depicted in Figure 3b. The bandgap values are 2.26 eV, 2.11 eV and 2.06 eV for the 0 %, 2 % and 5 % excess bismuth BFO samples, respectively. The bandgap decrement denotes the electrons and holes transportation responsible for the effective and enhanced photocatalytic activity of the materials [34].

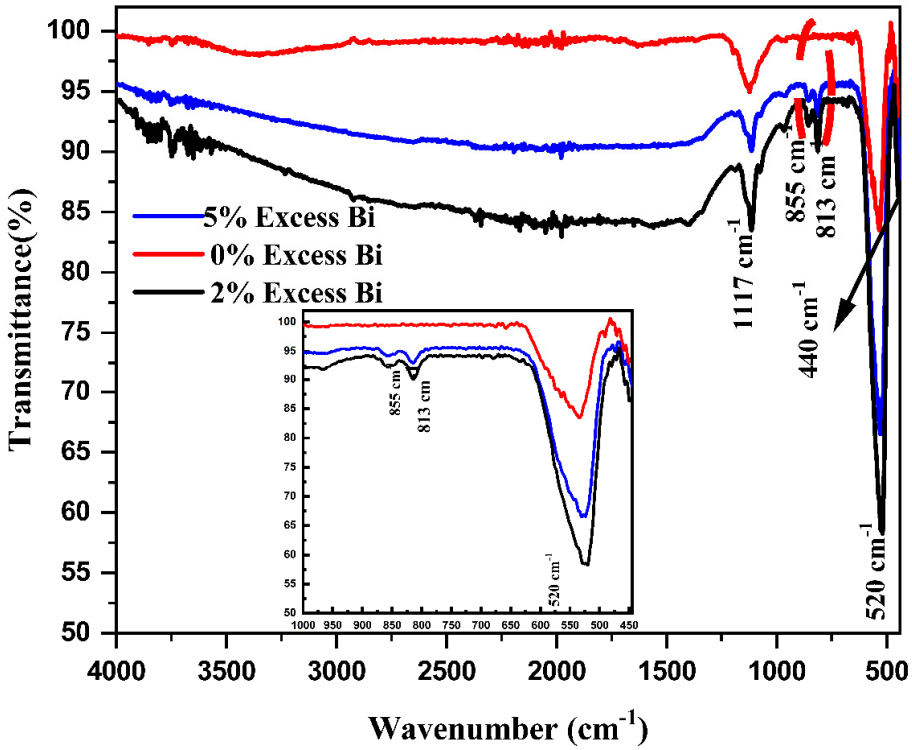

Figure 2. FT-IR spectrum of BFO (0%, 2% and 5% Excess Bi) nanoparticles.

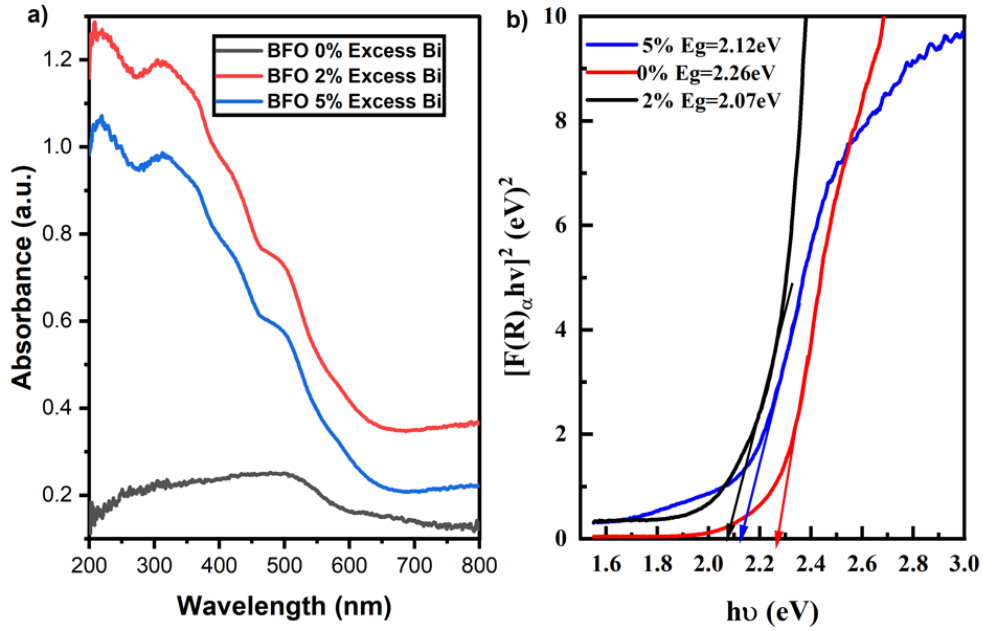

Figure 3. UV-Vis diffuse reflectance spectrum of BFO nanoparticles (**a**) and $[F(R)\alpha h\upsilon]^2$ versus photon energy spectrum (**b**).

3.4. PL Analysis

The photocatalytic efficiency is affected by the recombination rate of photoinduced charges, which was measured from photoluminescence analysis. The photoluminescence emission spectrum of green synthesised BFO nanoparticles has been provided in Figure 4. The emission spectra of excess bismuth BFO nanoparticle emissions were responsible for finding the rate of recombination of induced charges. The emission appeared at 587 nm in all the BFO nanoparticles with varying intensities depending on the bismuth contents, Figure 4 (inserted) [35,36]. The excitation wavelength was set at 333 nm during the experiment. The lowering intensity and separated charge carriers might be the responsible candidate for enhanced photocatalytic activity. The lower intensity values are well acknowledging the quantum size effect. The oxygen presence was shared by bismuth content that can produce enhanced activation on the surface. Without bismuth, their intensities were high, but the addition of bismuth to the Fe and O lattice decreased their intensities. The bismuth introduction to the BFO decreases the intensity and induces the charge carriers, which was reassured by previously reported work [37–40].

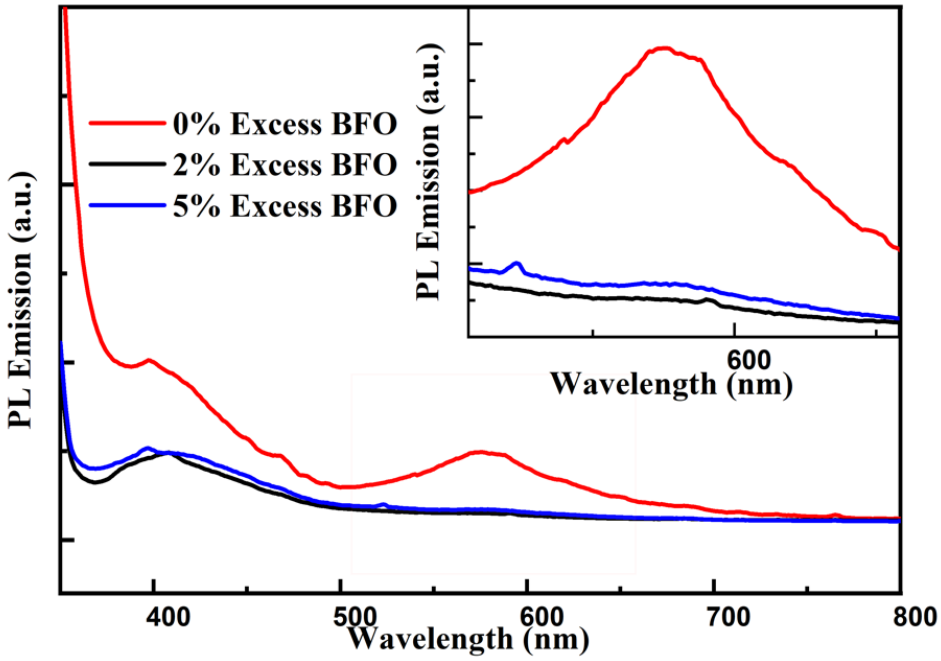

Figure 4. PL spectrum of $BiFeO_3$ (0%, 2% and 5% Excess Bi) nanoparticles.

3.5. FESEM Analysis

The surface properties of green synthesised BFO nanoparticles were observed from a field emission scanning electron microscope. The microscopic images of BFO nanoparticles with various percentages of bismuth context are shown in Figure 5. The 0% bismuth into the BFO nanoparticles revealed the cluster morphology with very smaller particles. Most of the particles are agglomerated and attached together. The 2% excess of bismuth into the BFO nanoparticles exhibited the spherical shape with polydisperse nanoparticles and their agglomeration level was found to be very minimum. The formed nanophase particles display a high surface area as well. The 5% excess of bismuth into the BFO nanoparticles emerged conjoint spherical shapes with larger grains, which were re-ensured by larger crystallite size and high bandgap energy. Altogether, the 2% excess of bismuth loaded BFO nanoparticles derived a better morphology and lowest crystallite and lower bandgap, which accelerated the photocatalytic activity.

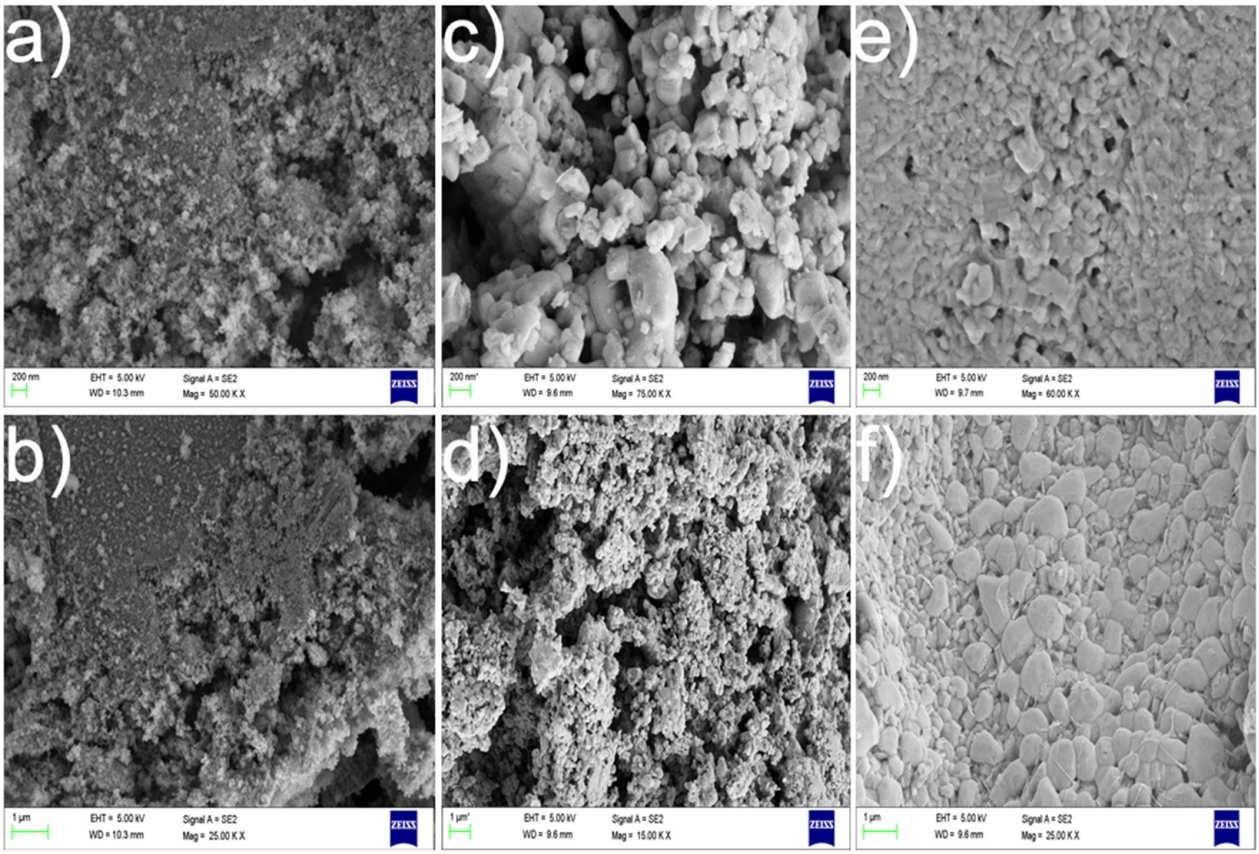

Figure 5. FESEM images of BFO (0% (**a**,**b**), 2% (**c**,**d**) and 5% (**e**,**f**) of excess bismuth BFO) samples.

3.6. XPS Analysis

The chemical composition and the valency of the green synthesised BFO nanoparticles were determined from X-ray photoelectron spectroscopy measurement. The XPS spectra of BFO nanoparticles wide (a), bismuth (b), iron (c), oxygen (d) and carbon (e) are displayed in Figure 6. The wide spectrum revealed that in the synthesised materials, bismuth, iron, oxygen and carbon are present in different valence states. The deep scan of the bismuth spectrum denotes the binding energy at 2 states; they are $4f_{7/2}$ and $4f_{5/2}$. The obtained binding energies were 158.51 eV at $4f_{7/2}$ and 163.86 eV at $4f_{5/2}$. In a BFO, +3 is a standard oxidation state of Fe, which is investigated in the Fe spectra of BFO. The binding energy of 710.3 eV and 724.7 eV were in the $2p_{3/2}$ and $2p_{1/2}$ states of the Fe spectrum [41–43]. The existing amount of iron is located at 718.3 eV, which is higher binding energy than the Fe $2p_{3/2}$ peak denoting the oxidation state of Fe not in Fe^{2+} but Fe^{3+}. The oxygen (O-1s) spectrum denotes the oxygen vacancy at 529.5 eV, which describes the bonding between Bi and Fe [44]. The carbon peaks displayed at 284.8 eV came from the honey solution [45]. The honey molecules consist of sucrose and fructose, which are responsible for the encapsulation/reduction in the title compound and reassured by FITR and UV analysis as well.

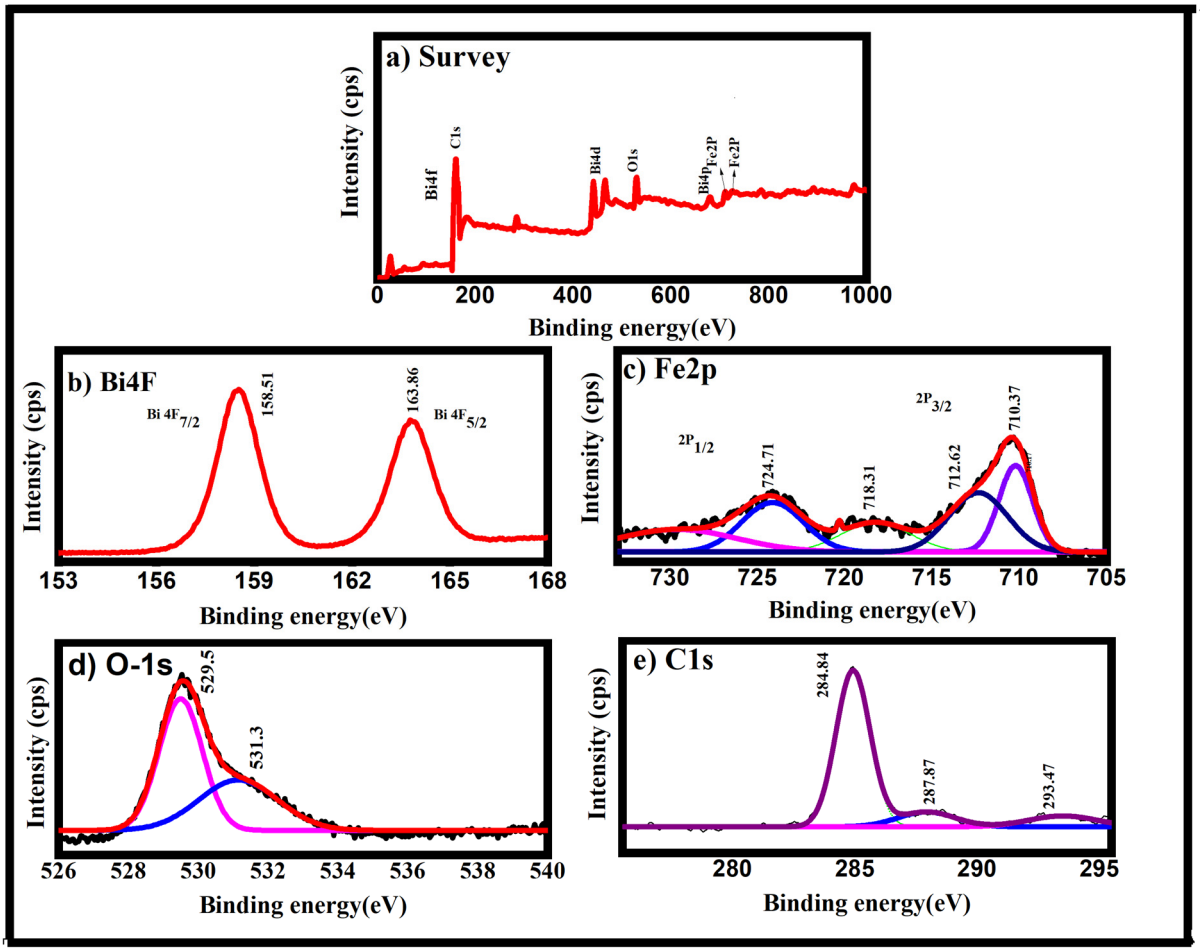

Figure 6. XPS survey (**a**), Bi-4f (**b**), Fe-2p (**c**), O-1s(**d**) and C-1s (**e**) spectrum of BFO (2% excess bismuth BFO) sample.

3.7. Antibacterial Activity

Microbes have been one of the deadliest things to humanity as they provoke a lot of death-spreading diseases. Therefore, researchers focused on a microbial resistance area, which is important worldwide. The present work describes the bacterial resistance of BFO nanoparticles, which was compared with a honey solution and amoxicillin drug. The optimised 2% excess of Bi in BFO nanoparticles emits the highest bacterial resistance than the rest of the nanoparticles (Figure 7). The 2% excess of Bi in the BFO nanoparticles zone of inhibitions is well-matched with standard drugs. Honey is a natural drug for microbial resistance, which inhibits bacterial migration. Based on the values, *E. coli* shows more sensitivity than *S. aureus* in both strains. The bacterial strain and nanoparticle interactions kill the bacteria via contact killing. The present work of BFO nanoparticles caused the Bi, Fe and dissolved oxygen ions, which interact with the cell wall of the bacteria [46,47]. These interactions may provoke free radical formations and cause cell wall damage, allowing hydrogen peroxide entry into the bacterial setup. Based on the obtained and previously reported work, BFO nanoparticles are highly appreciable in medical fields developing new drugs against contagious diseases.

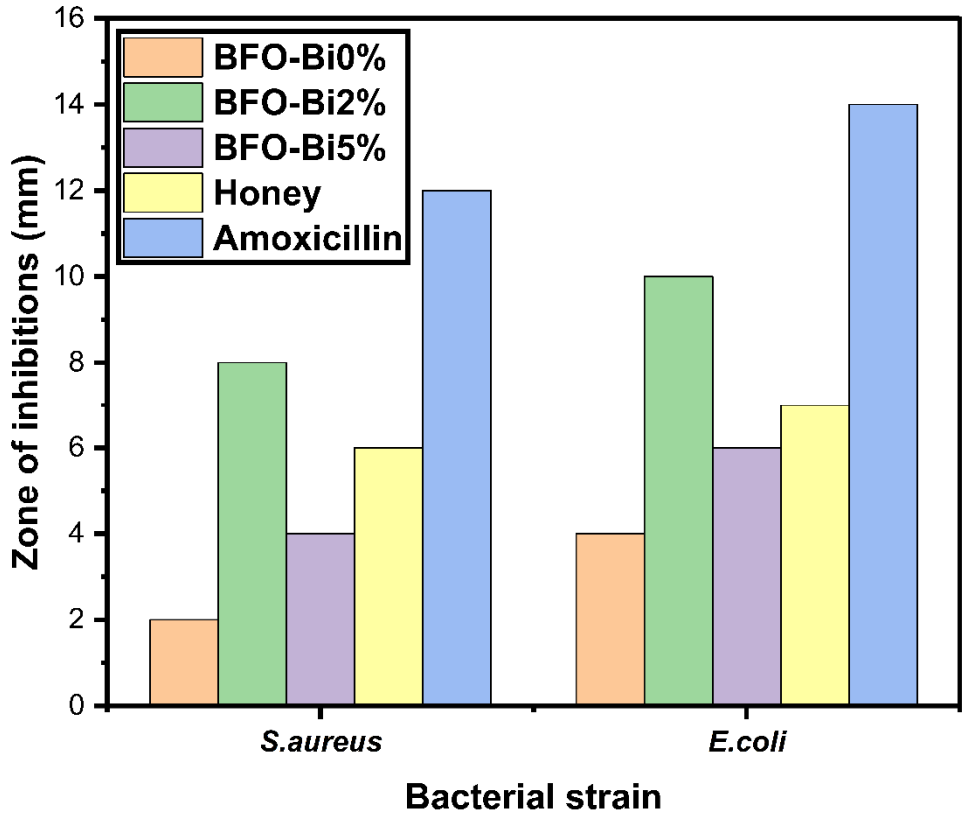

Figure 7. Antibacterial activity $BiFeO_3$ nanoparticles and honey solution.

3.8. Photocatalytic Dye Degradation

Photocatalytic dye degradation is one of the effective degradation methods to mineralise organic molecules [48–51]. The degradation depends on the initial dye concentration, catalyst dosage, dye solution pH value and different light sources. The BFO nanoparticles have a wide bandgap, which could act as a catalyst. The different nature of BFO nanoparticles (0%, 2% and 5% Bi content) were examined by photocatalyst activity to the MB dye (Figure 8). Among the tested nanoparticles, 2% BFO nanoparticles exhibit the highest activity compared to 0% and 5% Bi content BFO nanoparticles. The MB dye degradation is 5% while checking without any catalyst. The light interaction on the dye molecule surface increases the dissociation of dye compounds, but their output is very low compared to catalysts using photocatalytic activity. The degradation percentages of BFO nanoparticles are 66%, 81% and 68% of 0%, 2% and 5% Bi content BFO, respectively. The high content of Bi decreased the surface area and increased the crystallite size of the nanomaterials. The decreased surface area influences the catalytic activity. The 2% Bi content displays better catalytic activity than the 0% and 5% Bi content of BFO nanoparticles. The kinetics of the BFO nanoparticles were demonstrated in Figure 8b,c. The dark and light sources of photocatalytic activity have visually explained the nature of the catalyst. The 0% excess of Bi exhibits the highest degradation percentage than 2% and 5% of excess bismuth into the BFO nanoparticles in dark conditions. The light penetration on the catalyst surface increased the degradation. The photocatalytic dye degradation kinetics was evaluated by pseudo-first-order kinetics as follows [17]; $-\ln(C_t/C_0) = -kt$, where C_t is the vigorous concentration of MB at time t, C_0 is the primary concentration of MB, t is the degradation time, and k is the deceptive photocatalytic degradation constant. The kinetic rate of BFO nanoparticles was observed from pseudo-first-order kinetic, which was displayed in Figure 8c. The rate constant values are displayed in Figure 8c. The photocatalysis mechanism of BFO nanoparticles shows in Figure 8d. During the visible light source (xenon) interaction with the BFO nanoparticles, the electrons and holes are reoriented with the valence band (holes) and conduction band (electrons). The Bi content increases the surface

area of the BFO nanoparticles, which provokes catalytic activity. Hence 2% Bi excess BFO nanoparticles exhibited an enhanced catalytic activity than 0% Bi excess BFO nanoparticles. The single-phase and multi-phase BFO nanoparticles promote dye degradation towards the organic compounds. The visible light source illuminated on the BFO surface produces h^+ and e^-. These charges are separated by BFO nanoparticles and promote the higher-order catalytic activity in the MB dye solution. The Bi and BFO interface increased the charge separations and enhanced the water remediation capability over the catalyst surface. The excessive metal orientation on the BFO surface-induced the charge carriers more than pure BFO nanoparticles [52,53]. The charge carriers extend the lifetime of the recombination process and produce superoxides and hydroxides. These scavengers produce hydrogen peroxide (H_2O_2). The photogenerated holes, superoxides and hydroxides promote the degradation activity of MB dye solution. The above-mentioned mechanism equation is as follows.

$$BiFeO_3 + h\nu \rightarrow V.B^{h+} + C.B^{(e-)}$$

$$e^- + O_2 \rightarrow O_2{}^- + H_2O_2$$

$$h^+ + H_2O \rightarrow OH$$

$$O^{\cdot -}{}_2 + Dye \rightarrow degradation\ products$$

$$^{\cdot}OH + Dye \rightarrow nontoxic\ dye\ molecules$$

$$h^+ + Dye \rightarrow nontoxic\ dye\ molecules$$

The calculated values and their kinetics have embodied the improved photocatalytic activity. BFO nanoparticles produce higher photocatalytic activity due to the doping treatment, which depends on the crystallite size, morphology, particle size and bandgap of the materials.

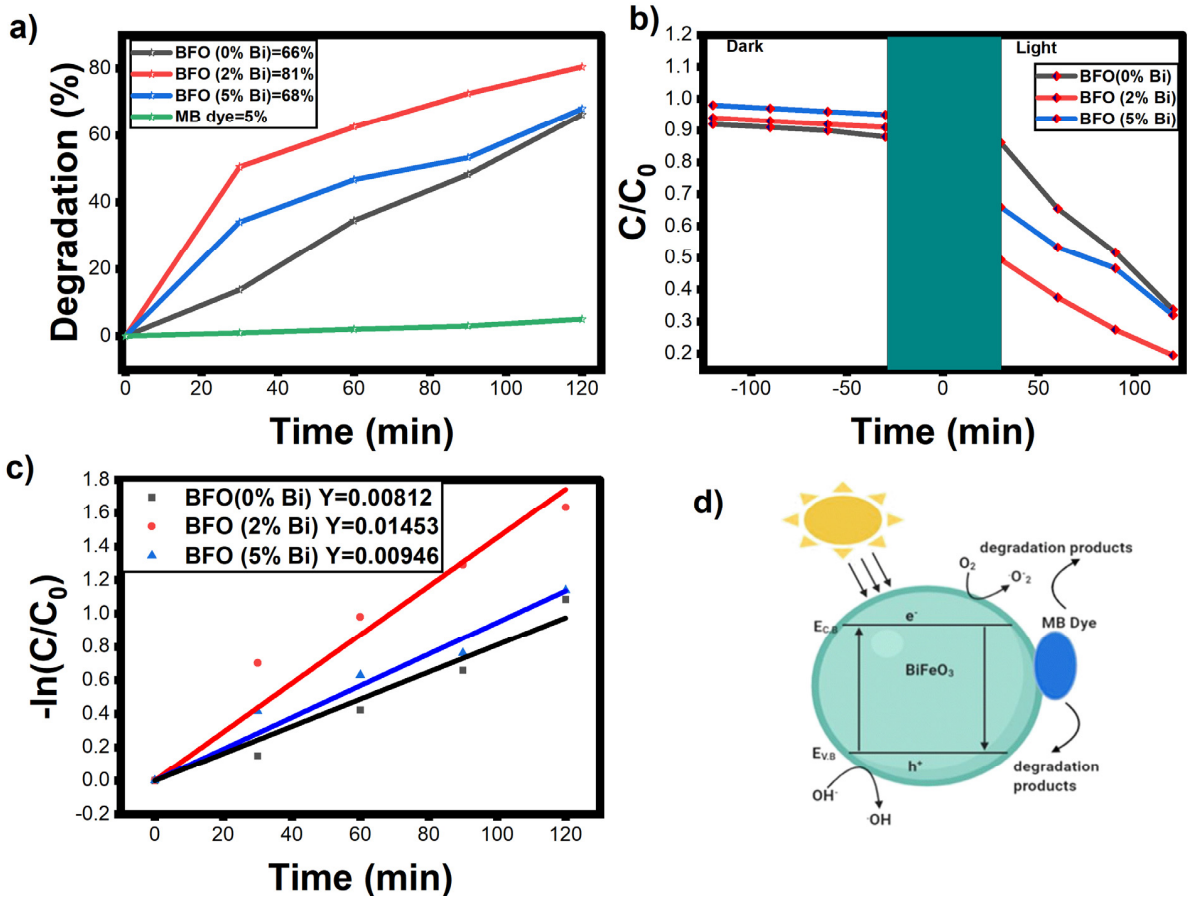

Figure 8. Photocatalytic dye degradation (**a**) efficiency, (**b**) C/C_0, (**c**) kinetics and (**d**) mechanism of the BFO nanoparticles.

The present work and previous reported BFO nanoparticles and their catalytic activity against various dyes are listed in Table 3. The light source, doping and crystallite size determine the catalytic activity. The large crystallite size reduced the surface area, which restricted hydroxyl formation. These activities decreased the dye degradation capacity. The UV light irradiation suppressed the electron-hole pair recombination, which provokes the high production of free radicals. Thus, the high production of free radicals parades the better catalytic activity. The BFO nanoparticles presented enhanced catalytic activity due to the metal trapping and increased the oxygen vacancies. Based on the previously reported work, the current BFO nanoparticles exhibit better catalytic activity in a limited time under visible light irradiation. The obtained results of BFO nanoparticles are a better replacement for wastewater treatment and catalytic activity on a larger scale.

Table 3. Photocatalytic dye degradation of BFO nanoparticles in different dyes.

S. No.	Nanoparticles	Dye	Source	Degradation %	Time (Min)	XRD (nm)	Reference
1.	BFO	RB	Visible	94	180	14.38	[54]
2.	BFO	RhB	Visible	62.3	60	50.63	[55]
3.	BFO	AR-85	Visible	60	60	57	[56]
4.	Ag-BFO	SY	Visible	84.4	240	-	[57]
5.	Ag-BFO	MB	Visible	91.2	240	-	[58]
6.	Se-BFO	CR	Visible	95	120	-	[58]
7.	BFO	DOX	UV	79	160	17.6	[59]
8.	BFO	MB	Visible	60	120	-	[60]
9.	BFO	MB	Sunlight	87	120	14	[22]
10.	BFO	MB	Sunlight	96.6	180	14	[22]
11.	Y-BFO	MB	Sunlight	92.6	120	14	[22]
12.	Y-BFO	MB	Sunlight	97.6	180	14	[22]
13.	BFO	TC	UV	92	180	29.46	[1]
14.	BFO	TC	Visible	99	180	29.46	[1]
15.	BFO	MB	Visible	66	120	19.2	Current work
16.	BFO	MB	Visible	81	120	10.51	Current work
17.	BFO	MB	Visible	68	120	26.8	Current work

4. Conclusions

The different amounts of excess bismuth content BFO nanoparticles were prepared by the auto combustion method. The honey is used as a green fuel to form the nanophase BFO nanoparticles and is accountable for capping and stabilising activities. The 2% excess bismuth BFO nanoparticles expressed better crystalline properties and reduced bandgap than other tested bismuth percentages in BFO nanoparticles. The reduced bandgap and lower intensity of the photoluminescence spectrum emanated from the photo-charge carriers and restricted the lifetime of recombination activity. XPS analysis observed that Bi, Fe and O valency and binding energies confirmed the optical potency and their charge carriers. The catalytic observation against the MB dye emanates the enhanced activity in 2% excess bismuth BFO nanoparticles. The degradation efficiency is 81% and their pseudo-first-order kinetic value is 0.01453 min^{-1} which was pointedly better than 0% and 5% of excess bismuth BFO nanoparticles. The antibacterial activity of BFO nanoparticles showed a more dynamic action against *E. coli* bacteria than *S. aureus*. Greener production of nanoparticles is a better way to remove/decrease pollution from the environment. Honey using BFO nanoparticles can be applied in higher production of the water recycling process and new drug designing fields.

Author Contributions: Conceptualization, M.S. and R.J.M.; methodology, R.J.M.; software, C.P.; validation, S.M.A.K., R.J.M. and M.S.; formal analysis, M.S.; investigation, R.J.M.; resources, S.M.W., M.R.S., M.A.I. and W.-C.L.; data curation, C.P.; writing—original draft preparation, M.S.; writing—review and editing, M.S.; visualization, M.S.; supervision, R.J.M.; project administration, R.J.M.; funding acquisition, S.M.W. All authors have read and agreed to the published version of the manuscript.

Funding: The authors are grateful to the Researchers Supporting Project No. (RSP-2021/326), King Saud University, Riyadh, Saudi Arabia.

Data Availability Statement: All research data used to assist the findings of this work are included within the manuscript.

Acknowledgments: The authors thank the management of Sadakathullah Appa College, Tirunelveli, Tamilnadu, India, for providing an opportunity to carry out this research. Manonmaniam Sundaranar University, Tirunelveli, Tamilnadu, India. The authors are grateful to the Researchers Supporting Project No. (RSP-2021/326), King Saud University, Riyadh, Saudi Arabia.

Conflicts of Interest: The authors declare no conflict of interest.

References

1. Rouhani, Z.; Karimi-Sabet, J.; Mehdipourghazi, M.; Hadi, A.; Dastbaz, A. Response surface optimization of hydrothermal synthesis of Bismuth ferrite nanoparticles under supercritical water conditions: Application for photocatalytic degradation of Tetracycline. *Environ. Nanotechnol. Monit. Manag.* **2019**, *11*, 100198. [CrossRef]
2. Zeljković, S.; Ivas, T.; Maruyama, H.; Nino, J.C. Structural, magnetic and optical properties of $BiFeO_3$ synthesized by the solvent-deficient method. *Ceram. Int.* **2019**, *45*, 19793–19798. [CrossRef]
3. Altaf, S.; Ali, K.; Khan, H.M.; Sardar, K.; Kamran, K.; Raza, M.A. Low Temperature Synthesis and Characterization of Bismuth Ferrite ($Bi_2Fe_4O_9$) Nanoparticles by Using Hydrothermal Method. *Dig. J. Nanomater. Biostructures* **2019**, *14*, 727–733.
4. Gautam, A.; Singh, K.; Sen, K.; Kotnala, R.; Singh, M. Crystal structure and magnetic property of Nd doped $BiFeO_3$ nanocrytallites. *Mater. Lett.* **2011**, *65*, 591–594. [CrossRef]
5. Priyadharsini, P.; Pradeep, A.; Sathyamoorthy, B.; Chandrasekaran, G. Enhanced multiferroic properties in La and Ce co-doped $BiFeO_3$ nanoparticles. *J. Phys. Chem. Solids* **2014**, *75*, 797–802. [CrossRef]
6. Muneeswaran, M.; Giridharan, N.V. Effect of Dy-substitution on the structural, vibrational, and multiferroic properties of $BiFeO_3$ nanoparticles. *J. Appl. Phys.* **2014**, *115*, 214109. [CrossRef]
7. Ishikawa, K.L. Nonlinear optical response of graphene in time domain. *Phys. Rev. B* **2010**, *82*, 201402. [CrossRef]
8. Arora, M.; Sati, P.C.; Chauhan, S.; Singh, H.; Yadav, K.L.; Chhoker, S.; Kumar, M. Structural, magnetic and optical properties of Bi1–xDyxFeO_3 nanoparticles synthesized by sol–gel method. *Mater. Lett.* **2013**, *96*, 71–73. [CrossRef]
9. Wang, L.; Han, Y.; Jia, G.; Zhang, C.; Liu, Y.; Liu, L.; Yin, K. Facile preparation, characterization and photocatalytic properties of multifunctional BiFeO3 nanocrystals. *J. Nanosci. Nanotechnol.* **2011**, *11*, 5207–5209. [CrossRef]
10. Feng, Y.-N.; Wang, H.-C.; Luo, Y.-D.; Shen, Y.; Lin, Y.-H. Ferromagnetic and photocatalytic behaviors observed in Cadoped $BiFeO_3$ nanofibres. *J. Appl. Phys.* **2013**, *113*, 146101. [CrossRef]
11. Chakrabarti, K.; Sarkar, B.; Ashok, V.D.; Das, K.; Chaudhuri, S.S.; Mitra, A.; De, S.K. Exchange bias effect in $BiFeO_3$-NiO nanocomposite. *J. Appl. Phys.* **2014**, *115*, 013906. [CrossRef]
12. Hasan, M.; Islam, M.F.; Mahbub, R.; Hossain, M.S.; Hakim, M.A. A soft chemical route to the synthesis of $BiFeO_3$ nanoparticles with enhanced magnetization. *Mater. Res. Bull.* **2016**, *73*, 179–186. [CrossRef]
13. Li, S.; Nechache, R.; Davalos, I.A.V.; Goupil, G.; Nikolova, L.; Nicklaus, M.; Laverdiere, J.; Ruediger, A.; Rosei, F. Ultrafast Microwave Hydrothermal Synthesis of $BiFeO_3$ Nanoplates. *J. Am. Ceram. Soc.* **2013**, *96*, 3155–3162. [CrossRef]
14. Fang, L.; Liu, J.; Ju, S.; Zheng, F.; Dong, W.; Shen, M. Experimental and theoretical evidence of enhanced ferromagnetism in sonochemical synthesized $BiFeO_3$ nanoparticles. *Appl. Phys. Lett.* **2010**, *97*, 242501. [CrossRef]
15. Khan, U.S.; Adeela, N.; Javed, K.; Riaz, S.; Ali, H.H.; Iqbal, M.; Han, X.F.; Naseem, S. Influence of cobalt doping on structural and magnetic properties of $BiFeO_3$ nanoparticles. *J. Nanoparticle Res.* **2015**, *17*, 429. [CrossRef]
16. Sharma, S.; Bhattacharya, A. Drinking water contamination and treatment techniques. *Appl. Water Sci.* **2017**, *7*, 1043–1067. [CrossRef]
17. Naushad, M.; Sharma, G.; Alothman, Z.A. Photodegradation of toxic dye using Gum Arabic-crosslinked-poly (acrylamide)/Ni (OH) 2/FeOOH nanocomposites hydrogel. *J. Clean. Prod.* **2019**, *241*, 118263. [CrossRef]
18. Ali, I.; Alharbi, O.M.L.; Alothman, Z.A.; Al-Mohaimeed, A.M.; Alwarthan, A. Modeling of fenuron pesticide adsorption on CNTs for mechanistic insight and removal in water. *Environ. Res.* **2019**, *170*, 389–397. [CrossRef]
19. Wabaidur, S.M.; Khan, M.A.; Siddiqui, M.R.; Otero, M.; Jeon, B.H.; Alothman, Z.A.; Hakami, A.A.H. Oxygenated functionalities enriched MWCNTs decorated with silica coated spinel ferrite—A nanocomposite for potentially rapid and efficient de-colorization of aquatic environment. *J. Mol. Liq.* **2020**, *317*, 113916. [CrossRef]
20. Alothman, Z.A. A Review: Fundamental Aspects of Silicate Mesoporous Materials. *Materials* **2012**, *5*, 2874–2902. [CrossRef]

21. Khan, M.A.; Alqadami, A.A.; Wabaidur, S.M.; Siddiqui, M.R.; Jeon, B.H.; Alshareef, S.A.; Alothman, Z.A.; Hamedelniel, A.E. Oil industry waste based non-magnetic and magnetic hydrochar to sequester potentially toxic post-transition metal ions from water. *J. Hazard. Mater.* **2020**, *400*, 123247. [CrossRef] [PubMed]
22. Satar, N.S.A.; Adnan, R.; Lee, H.L.; Hall, S.R.; Kobayashi, T.; Kassim, M.H.M.; Kaus, N.H.M. Facile green synthesis of ytrium-doped $BiFeO_3$ with highly efficient photocatalytic degradation towards methylene blue. *Ceram. Int.* **2019**, *45*, 15964–15973. [CrossRef]
23. Abushad, M.; Khan, W.; Naseem, S.; Husain, S.; Nadeem, M.; Ansari, A. Influence of Mn doping on microstructure, optical, dielectric and magnetic properties of $BiFeO_3$ nanoceramics synthesized via sol–gel method. *Ceram. Int.* **2019**, *45*, 7437–7445. [CrossRef]
24. Wang, Z.B.; Aldalbahi, A.; Ahamad, T.; Alshehri, S.M.; Feng, P.X. Preparation of $BiFeO_3$ and its photoelectric performance as photoanode of DSSC. *Ceram. Int.* **2021**, *47*, 27565–27570. [CrossRef]
25. Aliyu, A.; Srivastava, C. Correlation between growth texture, crystallite size, lattice strain and corrosion behavior of cop-per-carbon nanotube composite coatings. *Surf. Coat. Technol.* **2021**, *405*, 126596. [CrossRef]
26. Ranjithkumar, B.; Ramalingam, H.; Srinivas, C.; Magesh, G.; Rahale, C.S.; El-Metwaly, N.M.; Shekar, B.C. Natural fuels (Honey and Cow urine) assisted combustion synthesis of zinc oxide nanoparticles for antimicrobial activities. *Ceram. Int.* **2021**, *47*, 14475–14481. [CrossRef]
27. Ichangi, A.; Lê, K.; Queraltó, A.; Grosch, M.; Weissing, R.; Ünlü, F.; Chijioke, A.K.; Verma, A.; Fischer, T.; Surmenev, R.; et al. Electrospun $BiFeO_3$ Nanofibers for Vibrational Energy Harvesting Application. *Adv. Eng. Mater.* **2021**. [CrossRef]
28. Kossar, S.; Amiruddin, R.; Rasool, A. Study on thickness-dependence characteristics of bismuth ferrite (BFO) for ultraviolet (UV) photodetector application. *Micro Nano Syst. Lett.* **2021**, *9*, 1–10. [CrossRef]
29. Sharmila, M.; Jothi Mani, R.; Kader, A.; Ahmad, A.; Eldesoky, G.E.; Yahya, A.E.; Bahajjaj, A.A.A. Photocatalytic and Biological Activity of ZnO Nanoparticles Using Honey. *Coatings* **2021**, *11*, 1046. [CrossRef]
30. Chen, X.; Liu, B.; Li, X.; An, T.T.; Zhou, Y.; Li, G.; Wu-Smart, J.; Alvarez, S.; Naldrett, M.J.; Eudy, J.; et al. Identification of anti-inflammatory vesicle-like nanoparticles in honey. *J. Extracell. Vesicles* **2021**, *10*, e12069. [CrossRef]
31. Vishwakarma, A.K.; Tripathi, P.; Srivastava, A.; Sinha, A.; Srivastava, O. Band gap engineering of Gd and Co doped $BiFeO_3$ and their application in hydrogen production through photoelectrochemical route. *Int. J. Hydrogen Energy* **2017**, *42*, 22677–22686. [CrossRef]
32. Bharathkumar, S.; Sakar, M.; Vinod, K.R.; Balakumar, S. Versatility of electrospinning in the fabrication of fibrous mat and mesh nanostructures of bismuth ferrite ($BiFeO_3$) and their magnetic and photocatalytic activities. *Phys. Chem. Chem. Phys.* **2015**, *17*, 17745–17754. [CrossRef] [PubMed]
33. Aghdam, T.R.; Mehrizadeh, H.; Salari, D.; Tseng, H.H.; Niaei, A.; Amini, A. Photocatalytic removal of NOx over immobilized $BiFeO_3$ nanoparticles and effect of operational parameters. *Korean J. Chem. Eng.* **2018**, *35*, 994–999. [CrossRef]
34. Pattnaik, S.P.; Behera, A.; Martha, S.; Acharya, R.; Parida, K. Synthesis, photoelectrochemical properties and solar light-induced photocatalytic activity of bismuth ferrite nanoparticles. *J. Nanoparticle Res.* **2018**, *20*, 10. [CrossRef]
35. Prashanthi, K.; Thakur, G.; Thundat, T. Surface enhanced strong visible photoluminescence from one-dimensional multiferroic $BiFeO_3$ nanostructures. *Surf. Sci.* **2012**, *606*, L83–L86. [CrossRef]
36. Mishra, D.K.; Qi, X. Energy levels and photoluminescence properties of nickel-doped bismuth ferrite. *J. Alloys Compd.* **2010**, *504*, 27–31. [CrossRef]
37. Prashanthi, K.; Gupta, M.; Tsui, Y.Y.; Thundat, T. Effect of annealing atmosphere on microstructural and photoluminescence characteristics of multiferroic $BiFeO_3$ thin films prepared by pulsed laser deposition technique. *Appl. Phys. A* **2013**, *110*, 903–907. [CrossRef]
38. Miriyala, N.; Prashanthi, K.; Thundat, T. Oxygen vacancy dominant strong visible photoluminescence from $BiFeO_3$ nanotubes. *Phys. Status Solidi (RRL)—Rapid Res. Lett.* **2013**, *7*, 668–671. [CrossRef]
39. Li, J.; Huang, X.; Zhao, X.; Chen, L.J.; Yan, X.P. pH-Responsive Torpedo-Like Persistent Luminescence Nanoparticles for Autofluorescence-Free Biosensing and High-Level Information Encryption. *Angew. Chem.* **2021**, *133*, 2428–2435. [CrossRef]
40. Ramazanov, S.; Sobola, D.; Ţălu, Ş.; Orudzev, F.; Arman, A.; Kaspar, P.; Dallaev, R.; Ramazanov, G. Multiferroic behavior of the func-tionalized surface of a flexible substrate by deposition of Bi_2O_3 and Fe_2O_3. *Microsc. Res. Tech.* **2022**, *85*, 1300–1310. [CrossRef]
41. Tian, C.; Yao, Q.; Tong, Z.; Zhou, H.; Rao, G.; Deng, J.; Wang, Z.; Wang, J. Effects of Sm-doping on microstructure, magnetic and microwave absorption properties of $BiFeO_3$. *J. Rare Earths* **2021**, *39*, 835–843. [CrossRef]
42. Ahamad, T.; Aldalbahi, A.; Alshehri, S.M.; Alotaibi, S.; Alzahly, S.; Wang, Z.B.; Feng, P.X. Enhanced photovoltaic performance of dye-sensitized solar cells based Ag_2O doped $BiFeO_3$ hetrostructures. *Sol. Energy* **2021**, *220*, 758–765. [CrossRef]
43. Ramadan, W.; Feldhoff, A.; Bahnemann, D. Assessing the photocatalytic oxygen evolution reaction of $BiFeO_3$ loaded with IrO_2 nanoparticles as cocatalyst. *Sol. Energy Mater. Sol. Cells* **2021**, *232*, 111349. [CrossRef]
44. Amrillah, T.; Hermawan, A.; Yin, S.; Juang, J.Y. Formation and physical properties of the self-assembled BFO–CFO vertically aligned nanocomposite on a CFO-buffered two-dimensional flexible mica substrate. *RSC Adv.* **2021**, *11*, 15539–15545. [CrossRef]
45. Gajendiran, J.; Raj, S.G.; Kumar, G.R.; Gnanam, S.; Ramya, J.R.; Senthil, V.P. Photoluminescence Properties and Antibacterial Activity of $BiFeO_3$ and $BiFeO_3$-$CoFe_2O_4$ Composite. *J. Electron. Mater.* **2022**, *51*, 8–16. [CrossRef]
46. Rameshkumar, C.; Gayathri, R.; Subalakshmi, R. Synthesis and characterization of undopped bismuth ferrite oxide nanoparticles for the application of cancer treatment. *Mater. Today Proc.* **2021**, *43*, 3662–3665. [CrossRef]

47. Chouker, M.A.; Abdallah, H.; Zeiz, A.; El-Dakdouki, M.H. Host-quest inclusion complex of quinoxaline-1, 4-dioxide derivative with 2-hydroxypropyl-β-cyclodextrin: Preparation, characterization, and antibacterial activity. *J. Mol. Struct.* **2021**, *1235*, 130273. [CrossRef]
48. Ahmed, H.M.; Roy, A.; Wahab, M.; Ahmed, M.; Othman-Qadir, G.; Elesawy, B.H.; Khandaker, M.U.; Islam, M.N.; Emran, T.B. Applications of nanomaterials in agri food and pharmaceutical industry. *J. Nanomater.* **2021**, *2021*, 1472096. [CrossRef]
49. Nabavi, S.; Behzad, S. Herbal Drugs and Natural Products in the light of Nanotechnology and Nanomedicine for Developing Drug Formulations. *Mini-Rev. Med. Chem.* **2021**, *21*, 302–313. [CrossRef]
50. Roy, A.; Ananda Murthy, H.C.; Ahmed, H.M.; Islam, M.N.; Prasad, R. Phytogenic Synthesis of Metal/Metal Oxide Nanoparticles for Degradation of Dyes. *J. Renew. Mater.* **2022**, *10*, 1911. [CrossRef]
51. Shimi, A.K.; Ahmed, H.M.; Wahab, M.; Katheria, S.; Wabaidur, S.M.; Eldesoky, G.E.; Islam, M.A.; Rane, K.P. Synthesis and Applications of Green Synthesized TiO_2 Nanoparticles for Photocatalytic Dye Degradation and Antibacterial Activity. *J. Nanomater.* **2022**, *2022*, 7060388. [CrossRef]
52. Pan, Z.; Liu, M.; Zhang, G.; Zhuzhang, H.; Wang, X. Molecular Triazine–Heptazine Junctions Promoting Exciton Dissociation for Overall Water Splitting with Visible Light. *J. Phys. Chem. C* **2021**, *125*, 9818–9826. [CrossRef]
53. Pan, Z.; Zhao, M.; Zhuzhang, H.; Zhang, G.; Anpo, M.; Wang, X. Gradient Zn-Doped Poly Heptazine Imides Integrated with a van der Waals Homojunction Boosting Visible Light-Driven Water Oxidation Activities. *ACS Catal.* **2021**, *11*, 13463–13471. [CrossRef]
54. Siddique, M.; Khan, N.M.; Saeed, M. Photocatalytic Activity of Bismuth Ferrite Nanoparticles Synthesized via Sol-Gel Route. *Z. Für Phys. Chem.* **2019**, *233*, 595–607. [CrossRef]
55. Puhan, A.; Bhushan, B.; Satpathy, S.; Meena, S.S.; Nayak, A.; Rout, D. Facile single phase synthesis of Sr, Co co-doped $BiFeO_3$ nanoparticles for boosting photocatalytic and magnetic properties. *Appl. Surf. Sci.* **2019**, *493*, 593–604. [CrossRef]
56. Ponraj, C.; Vinitha, G.; Daniel, J. Photocatalytic degradation of acid red-85 dye by nickel substituted bismuth ferrite nanoparticles. *Mater. Res. Express* **2019**, *6*, 084006. [CrossRef]
57. Jaffari, Z.; Lam, S.-M.; Sin, J.-C.; Zeng, H. Boosting visible light photocatalytic and antibacterial performance by decoration of silver on magnetic spindle-like bismuth ferrite. *Mater. Sci. Semicond. Process.* **2019**, *101*, 103–115. [CrossRef]
58. Irfan, S.; Zhuanghao, Z.; Li, F.; Chen, Y.-X.; Liang, G.-X.; Luo, J.-T.; Ping, F. Critical review: Bismuth ferrite as an emerging visible light active nanostructured photocatalyst. *J. Mater. Res. Technol.* **2019**, *8*, 6375–6389. [CrossRef]
59. Dumitru, R.; Ianculescu, A.; Păcurariu, C.; Lupa, L.; Pop, A.; Vasile, B.S.; Surdu, V.-A.; Manea, F. $BiFeO_3$-synthesis, characterization and its photocatalytic activity towards doxorubicin degradation from water. *Ceram. Int.* **2019**, *45*, 2789–2802. [CrossRef]
60. Duan, Q.; Kong, F.; Han, X.; Jiang, Y.; Liu, T.; Chang, Y.; Zhou, L.; Qin, G.; Zhang, X. Synthesis and characterization of morphology-controllable $BiFeO_3$ particles with efficient photocatalytic activity. *Mater. Res. Bull.* **2019**, *112*, 104–108. [CrossRef]